Simulation of the Temperatures in Permanently Shadowed Region of the Crater Shackleton and Implications to In-Situ Detection

Zhengling Yin , Niutao Liu , *Member, IEEE*, and Ya-Qiu Jin , *Life Fellow, IEEE*

Abstract—In China's Chang'e 7 mission, a miniflyer will be carried for in-situ water ice measurement in permanently shadowed regions (PSRs) around the lunar south pole. The extreme cold environment within PSRs causes serious challenges for the safety of the miniflyer. Predication of temperatures in PSR is critical for designing the internal heating system and the heat source capacity. Conducting in-situ detection mission in relatively warm temperature can reduce the threat of the cold environment and save energy to maintain a suitable operation temperature for payloads. Since the polar-orbiting satellite lunar reconnaissance orbiter passes over the same location in the polar region with intervals of about a month, the temporally continuous observation is unavailable. Simulation is necessary to determine the temporally continuous temperatures of PSR during the mission. In this article, a numerical model of the temperatures in PSR is presented. The ray tracing approach is used to calculate the shadowing effect of terrain on scattered sunlight and thermal radiation. The PSR temperatures are simulated with the one-dimensional heat conduction equation. Simulated temperatures are compared with Diviner data for validation. The spatial and temporal temperature distributions of PSRs in crater Shackleton, which is the preferred landing site for the Chang'e 7 mission, are simulated from 2026 to 2028. The simulated temperature in high temporal resolution of one Earth hour can be applied to analyzing diurnal and seasonal temperatures in PSRs and is helpful for thermal management and design of the internal heating system. The time windows with relatively warm temperature in PSR at regions with slope angles less than 5° are recommended to save energy and reduce the hazards of the extremely cold environment.

Index Terms—Mini-flyer, Moon, permanently shadowed region (PSR), temperature, thermal management.

I. INTRODUCTION

SOME lunar polar regions remaining permanently shaded are called permanently shadowed regions (PSRs). The temperatures in PSR keep extremely cold, making it possible to preserve water ice [1], [2], [3], [4]. Water ice in lunar regolith is important in future lunar exploration missions, as water resources provide essential support for human activities [5], [6]. China's Chang'e 7 mission is planning to carry a Mini-flyer to conduct in-situ exploration within PSRs [7], [8], [9].
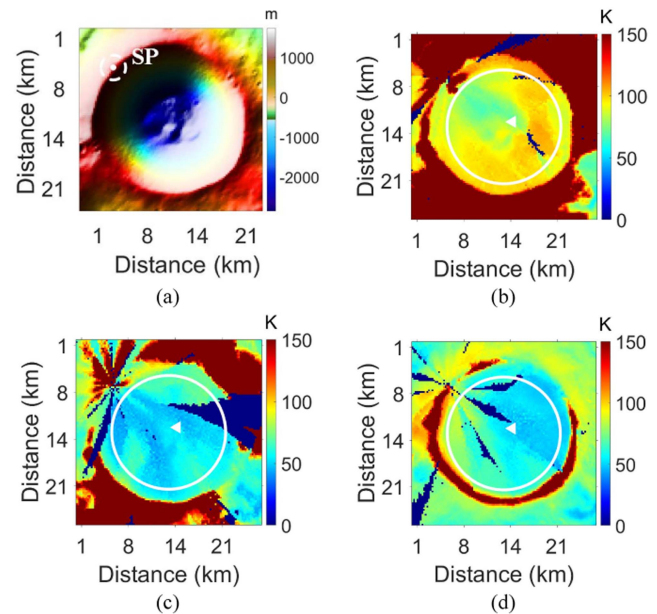
Fig. 1. Topography and diviner data of crater Shackleton [2]. (a) DEM of Shackleton, with the south pole marked by a white point (SP). The central latitude and longitude of Shackleton are 89.6°S and 129.2°E. It has a diameter of approximately 20.9 km. (b) Temperature data at 12:00 in summer. (c) Temperature data at 12:00 in winter. (d) Temperature data at 0:00 in summer.

The extreme cold-temperature, typically lower than 110 K [1], [2], [3], [4], [10], in the PSRs may cause a great threat to the security of miniflyer payloads, which typically operates under temperatures from 273 K to 313 K [11]. To work in the cold environment of PSR, heat sources are needed to keep the payload warm. The power to maintain the temperature depends on the PSR temperature of the landing site during the mission.

It has been observed that there are seasonal and diurnal variations of temperature in the PSRs. Take crater Shackleton, the preferred landing site for the Chang'e 7 mission [12], as an example. Fig. 1(a) shows the digital elevation model (DEM) of crater Shackleton from lunar orbiter laser altimeter (LOLA) onboard lunar reconnaissance orbiter (LRO) [13], with the south pole marked by a white point (SP). Its central latitude and longitude are 89.6°S and 129.2°E. Shackleton has a diameter of approximately 20.9 km [2]. Fig. 1(b) and (c) show the Diviner data of crater Shackleton at 12:00 in summer and winter respectively.

The Diviner data divided by local time are compiled by Williams et al. [2], [14]. In Fig. 1(b) and (c), the average PSR temperature in summer daytime is 90 K. The area of PSR is approximately outlined by a white circle. The average daytime temperature of PSR in winter becomes 54 K, which has a seasonal temperature difference of about 36 K. Fig. 1(c) shows the Diviner data at 0:00 in summer. The average nighttime temperature in summer is about 59 K. The diurnal variation in average PSR temperature is about 31K. For a point located in the region within the PSR, which is marked with a white triangle in Fig. 1(b), (c) and (d), its seasonal difference of the temperature can reach about 50 K, and its diurnal variation in temperature is about 53 K. Such great diurnal and seasonal temperature variations may impact the design of battery capacity, the selection of heat sources, and the design of thermal control schemes.

Maintaining a relatively warm temperature in a cold environment requires more energy. The increase in the miniflyer's battery capacity for more energy will lead to an increase in the battery mass, which will incur significant costs. Conducting tasks in the relatively warm temperatures of PSRs is advantageous for energy conservation and also can reduce the threats posed by extremely cold temperatures to electronic components and thermal fatigue under large temperature difference.

In addition, scattered and radiative heat fluxes from different directions vary within the PSRs, resulting in different heat flux intensities on the surfaces of the miniflyer with varied orientations. Surfaces with lower heat flux reception require more power to maintain the temperature. Therefore, conducting research on the spatiotemporal temperature distribution in PSRs is of importance for the design of the heat source and the selection of the mission's time.

Since the Diviner data are from the past, it cannot represent future temperatures. In addition, LRO is a polar-orbiting satellite that passes over the south pole approximately every two hours and covers the polar region about once a month. The next pass over the same location in the polar region occurs at intervals of approximately one month. Therefore, temporally continuous observational data at the same location are lacking to predict future temperature variations within Shackleton. A physical model is required to determine the temperatures during the mission. The numerically simulated temperatures with high time resolution of one Earth hour are presented in this article. The spatial and temporal variations of PSR temperatures during the Chang'e 7 mission are predicted and the heat fluxes of scattered and radiated from different directions within PSRs are simulated as well. Seasonal and diurnal temperature variations on the flat floor are presented. The time window with relatively warm temperature is recommended for the in-situ detection.

The rest of this article is organized as follows. Section II introduces the simulations of temperatures in PSRs. Section III analyzes the spatial and temporal temperature distributions and heat fluxes from different directions. The time windows with relatively warm temperature in PSR are predicted. Finally, Section IV concludes this article.
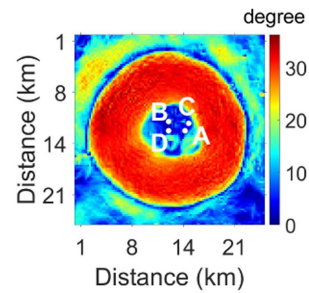

Fig. 2. Slope map of crater Shackleton, points A–D are located at the flat crater floor.

II. SIMULATION OF PSR TEMPERATURES

A. Data Sets

In June 2009, the LRO was launched. LRO carried the Diviner Lunar Radiometer to investigate the global solar reflectance and lunar thermal infrared emission [15]. This instrument encompasses a frequency range spanning nine spectral channels from 0.3 to 400 μm. Among the nine channels, channels 6 to 9 focus on capturing the lunar thermal emissions and subsequently deriving brightness temperatures (TB). Since the infrared emission can hardly penetrate the lunar regolith, the IR TB data can be used to represent the lunar surface temperature. However, due to the lack of temporally continuous observational data for crater Shackleton and the data loss in low-temperature regions caused by low signal-to-noise ratios, this article uses the temperature data compiled by Williams et al. [2], [14] for validation. Williams et al. compiled the first 5.5 years of Diviner observations of lunar poles into a gridded data set, and divided the data set according to season, subsolar longitude, and local time. Bolometric brightness temperatures are then determined from the binned radiance measurements from Diviner channels 3–9, and are averaged during the binning. The bolometric brightness temperatures are used in this article. The projection method is polar stereographic, with a spatial resolution of 240 m/pixel [2], [14].

The topography of the Moon is constructed by DEM from LOLA onboard LRO. The resolution of the DEM data is 240 m/pixel. For the sake of safety, the miniflyer needs to land in flat areas. Based on the slope map of crater Shackleton in Fig. 2, four points marked as A, B, C, and D are selected for temperature simulations, whose slopes are all less than 5°. The longitude and latitude for point A, B, C, D are (89.6°S, 123.8°E), (89.7°S, 125.0°E), (89.6°S, 118.8°E), and (89.7°S, 130.4°E), respectively.

B. Ray Tracing

Ray tracing is employed to assess the shadow of direct solar illumination, scattered sunlight, and thermal radiation by the lunar terrain. The lunar surface is constructed by DEM data from LOLA [12], which can be accessed through the geosciences node of the planetary data system. The lunar surface is divided into small triangular meshes. Each quadrilateral formed by four adjacent DEM data points is further divided into two triangular

meshes: the upper left and lower right sections. The Sun is treated as a point light source emitting parallel rays. To determine whether scattered sunlight and thermal radiation are obstructed, the centers of the two triangular meshes are used to trace the ray's path. All meshes will be designated as emitting meshes for ray tracing. Rays originate from the emitting mesh and travel to all other meshes. If a ray is blocked in its path to a target mesh, then the tracing process ends, and the emitting mesh will not be considered to contribute heat flux to that target mesh. On the other hand, if the ray reaches the target mesh, parameters such as propagation distance, emission angle, and incident angle are recorded.

C. One-Dimensional Heat Conduction Equation

The temperature of lunar regolith is simulated using the one-dimensional (1-D) heat conduction equation [16]

$$\rho C \frac{\partial T}{\partial t} = \frac{\partial}{\partial z}\left(K\frac{\partial T}{\partial z}\right) \tag{1}$$

where T (K) represents the regolith temperature at depth z, K (Jkg^{-1}K^{-1}) represents the thermal conductivity, and C (Wm^{-1}K^{-1}) represents heat capacity. Regolith density ρ(kgm^{-3}) experiences exponential growth with increasing depth [16]

$$\rho(z) = \rho_d - (\rho_d - \rho_s)e^{-\frac{z}{H}} \tag{2}$$

where ρ_s represents the density of the regolith on the lunar surface, and ρ_d is the density of the regolith at the depth far exceeds H. There is $\rho_s = 1100$ kgm^{-3}, and $\rho_d = 1800$ kgm^{-3}.

The upper and lower boundary conditions of the 1-D heat conduction equation can be written as [17]:

$$K(z,T)\frac{\partial T}{\partial z}|_{z=0} = \text{TSI}(1-\overline{A})\cos^+\theta_j + I_R + I_S - \overline{e}\sigma T_S^4 \tag{3a}$$

$$K(z,T)\frac{\partial T}{\partial z}|_{z=-\infty} = -J_0 \tag{3b}$$

where $K(z,T)\frac{\partial T}{\partial z}|_{z=0}$ represents the heat flux transmitted between the surface and the subsurface. TSI$(1-\overline{A})\cos^+\theta_j$ represents the surface solar flux, where TSI is the real-time total solar irradiance, and θ_j is the solar incidence angle at mesh j. I_R and I_S are the received thermal radiation and scattered sunlight respectively. The average emissivity $\overline{e}$ for all directions is set to 0.95 [1], [16], [18]. σ is the Stefan–Boltzmann constant. T_S is the surface temperature.

While in the lower boundary conditions, the internal heat flux J_0 is small. Paige et al. [1] had investigated the impact of J_0. They proposed that the internal heat flux might play a role in maintaining the overall heat balance of PSRs, yet it is not the primary factor when compared to the heating from scattered sunlight and thermal radiation. Therefore, J_0 is set to 0 W/m^2 in this article. The Newton's method is used to solve the upper boundary condition, and the 1-D heat conduction equation is solved by the finite-difference time-domain method. To ensure convergence, the finite-difference time-domain method is run for over 100 lunations.

D. Real-Time Solar Illumination and Thermal Radiation

In the calculation of surface solar flux TSI$(1-\overline{A})\cos^+\theta_j.\theta_j$ is the solar incidence angle at mesh j. When θ_j exceeds 90° or the incident sunlight is blocked by terrain, $\cos^+\theta_j$ is set to 0. Otherwise, $\cos^+\theta_j = \cos\theta_j$[10]. TSI depends on the Sun–Moon distance d_s. When the Sun–Moon distance is 1 AU, *TSI* is 1371 W/m^2 [19]. The equation of TSI can be written as [20]:

$$\text{TSI} = 1371/d_s^2 \tag{4}$$

where d_s is in AU.

The heat flux of direct thermal radiation, I_{Ri}, received by mesh i from all other meshes is [10]

$$I_{Ri} = \frac{\sum_{j\neq i} H_{ij}}{S_i} \tag{5}$$

$$H_{ij} = \frac{e(\theta_e)\sigma T_j^4 \times S_j \times \cos(\theta_i)}{2\pi d_{ij}^2} \cdot S_i \tag{6}$$

where the emission angle θ_e is the angle between the normal vector of the emitting mesh j and the direction of the heat flux from mesh j to mesh i. T_j is the surface temperature of mesh j, S_i and S_j are the areas of triangular meshes i and j, θ_i is the incidence angle of the heat flux at mesh i, and d_{ij} is the distance between mesh i and mesh j.

The heat flux of single-bounce scattered sunlight, I_{Si}, received by mesh i from all other meshes is

$$I_{Si} = \frac{\sum_{j\neq i} P_{ij}}{S_i} \tag{7}$$

$$P_{ij} = \text{TSI} \times \cos(\theta_j) \times A(\theta_j) \times S_j \times \frac{G(\theta_j,\theta_{ij}^e)}{2\pi d_{ij}^2} \times \cos(\theta_i)$$

$$\times (1-\overline{A}(\theta_i)) \times S_i \tag{8}$$

where $A(\theta_j) \times G(\theta_j,\theta_{ij}^e)$ represents bidirectional reflectance [21]. An isotropic scattering model with $G = 1$ is used [10].

The radiation and scattered heat flux to the miniflyer can be calculated with the simulated PSR temperatures. The thermal radiation I_{Ri}^0 and scattered sunlight I_{Si}^0 from lunar surface to the miniflyer can be written as

$$I_{Ri}^0 = \sum_{j\neq i} H_{ij}^0 \tag{9}$$

$$H_{ij}^0 = \frac{e(\theta_e)\sigma T_j^4 \times S_j}{2\pi d_{ij}^2} \tag{10}$$

$$I_{Si}^0 = \sum_{j\neq i} P_{ij}^0 \tag{11}$$

$$P_{ij}^0 = \text{TSI} \times \cos(\theta_j) \times A(\theta_j) \times S_j \times \frac{G(\theta_j,\theta_{ij}^e)}{2\pi d_{ij}^2}. \tag{12}$$

E. Thermophysical Parameters

The thermophysical parameters in extremely low temperature in PSR are different from that in high temperatures out of the PSR. The thermophysical parameters suitable for low temperature are selected for simulation.

The heat capacity varies with temperature, as observed in the measurements [16]. A polynomial-fitted heat capacity derived from sample measurements is utilized, specifically suitable for the low-temperature environment of PSR [22] (13) shown at the bottom of this page, with $C_0 = -3.6125\,\mathrm{Jkg^{-1}K^{-1}}$, $C_1 = 2.7431\,\mathrm{Jkg^{-1}K^{-2}}$, $C_2 = 2.3616 \times 10^{-3}\,\mathrm{Jkg^{-1}K^{-3}}$, $C_3 = -1.2340 \times 10^{-5}\,\mathrm{Jkg^{-1}K^{-4}}$ $C_4 = 8.9093 \times 10^{-9}\,\mathrm{Jkg^{-1}K^{-5}}$, $C_1' = -0.55 \times 10^{-1}\,\mathrm{Jkg^{-1}K^{-2}}$, $C_2' = 9.715 \times 10^{-2}\,\mathrm{Jkg^{-1}K^{-3}}$, $C_3' = -1.261 \times 10^{-3}\,\mathrm{Jkg^{-1}K^{-4}}$ $C_4' = 7.709 \times 10^{-6}\,\mathrm{Jkg^{-1}K^{-5}}$, $C_5' = -2.182 \times 10^{-8}\,\mathrm{Jkg^{-1}K^{-6}}$, and $C_6' = 2.212 \times 10^{-11}\,\mathrm{Jkg^{-1}}$ $\mathrm{K^{-7}}$.

The thermal conductivity significantly affects temperatures in subsurface and nighttime lunar surface temperatures. Martinez and Siegler [23] proposed a new thermal conductivity model suitable for both extremely low-temperature environments in PSR and high-temperature environments exposed to direct sunlight. To study the impact of thermal conductivity in PSR, Yin et al. [10] simulated the PSR temperature at night in winter with the thermal conductivities of [23] and [16]. It was found that the simulated PSR temperature with Martinez et al.'s model is closer to the Diviner data than the temperature simulated with Hayne et al.'s model at night in winter. Therefore, Martinez et al.'s model is employed here to predict the temperature distribution in Shackleton

$$k_{eff}(T, \rho) = (A_1\rho - A_2)k_{am}(T) + (B_1\rho - B_2)T^3 \quad (14)$$

where $A_1 = 5.0821 \times 10^{-6}$, $A_2 = 5.1 \times 10^{-3}$, $B_1 = 2.0022 \times 10^{-13}$, and $B_2 = 1.953 \times 10^{-10}$; $k_{am}(T)$ is the temperature-dependent solid conduction component given by $k_{am}(T) = A_{am} + B_{am}T^{-4} + C_{am}T^{-3} + D_{am}T^{-2} + E_{am}T^{-1} + F_{am}T + G_{am}T^2 + H_{am}T^3 + I_{am}T^4$, where $A_{am} = -0.203297$, $B_{am} = -11.472$, $C_{am} = 22.5793$, $D_{am} = -14.3084$, $E_{am} = 3.41742$, $F_{am} = 0.01101$, $G_{am} = -2.8049 \times 10^{-5}$, $H_{am} = 3.35837 \times 10^{-8}$, and $I_{am} = -1.40021 \times 10^{-11}$ [23].

In addition, emissivity has significant impact on daytime temperatures in PSRs. In previous work, the emissivity was set as a constant [1], [18]. Paige et al. [1] found that simulated daytime temperatures in PSRs with isotropic emissivity were approximately 15 K lower than the Diviner data, which may be attributed to directionally anisotropic infrared emission from rough crater walls. In order to close the discrepancy between the simulation and the Diviner data [1], [17] used the anisotropy emissivity that varies with the emission angle [17]

$$e(\theta) = e_F(\theta)^2 / 0.942 \quad (15)$$

where $e_F(\theta)$ is the Fresnel emissivity. Division by the adjustment factor 0.942 increases the amplitude of the emissivity, giving $e(0°) = 1$. The Fresnel emissivity is calculated as

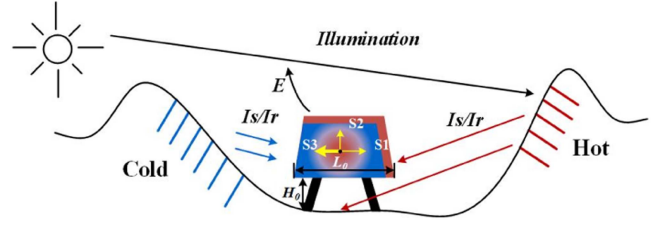$$e_F(\theta) = (e_h(\theta) + e_v(\theta))/2 \quad (16)$$

Fig. 3.   Schematic diagram of thermal equilibrium of the Chang'E-7 miniflyer. The yellow arrows represent the conductive heat fluxes from internal heat sources.

with

$$\begin{aligned} e_h(\theta) &= 1 - R_h(\theta) \\ e_v(\theta) &= 1 - R_v(\theta). \end{aligned} \quad (17)$$

Here, $R_h(\theta)$ and $R_v(\theta)$ are the Fresnel reflectivities of the horizontal and vertical polarizations at emission angle θ.

To compare the effects of emissivity on temperature, Yin et al. [10] used isotropic and anisotropic emissivities to simulated daytime temperatures within the PSRs. By comparing the simulations with Diviner data, it was found that the PSR temperatures simulated with anisotropic emissivity are closer to the Diviner data than those simulated with isotropic emissivity. Anisotropic emissivity is used to simulated the temperature in this article.

III. SIMULATION AND ANALYSIS

During the daytime, the miniflyer's surface temperature depends on the scattered sunlight and thermal radiation from the surrounding terrain, the conductive heat flux from internal heat sources of miniflyer, and the thermal emission to the space, as shown in Fig. 3. The miniflyer's surfaces S1 and S2 facing the sunlit area can receive more scattered sunlight and thermal radiation. As a result, S1 and S2 require less conductive heat flux from internal heat sources to maintain a suitable temperature. Conversely, the surface S3 facing away from the sunlit area receives most of its heat flux from the cold-temperature regions in shadow, resulting in less received heat fluxes. Consequently, S3 needs more internal heat flow to maintain a suitable temperature. The temperature in the sunlit region and the PSR experiences spatio-temporal variations during a lunation, which will affect the heat flux received by different surfaces of the miniflyer.

The spatio-temporal temperature variations within the Shackleton crater are analyzed with simulation. The south pole is located in the upper left corner of the crater, as shown in Fig. 1(a). Therefore, the area and the position of sunlit regions on Shackleton's crater walls will change with local time, resulting in diurnal temperature variations in and out of PSRs.

Fig. 4 shows the Diviner data, the simulated surface temperatures and sunlit regions of Shackleton at different times during the summer. The local time of Fig. 4(a), (c), and (e) is 14:30 and the local time of Fig. 4(b), (d), and (f) is 17:30.

$$C = \begin{cases} C_1'T + C_2'T^2 + C_3'T^3 + C_4'T^4 + C_5'T^5 + C_6'T^6 & 10\mathrm{K} < T < 200\mathrm{K} \\ C_0 + C_1T + C_2T^2 + C_3T^3 + C_4T^4 & 200\mathrm{K} < T < 400\mathrm{K} \end{cases} \quad (13)$$
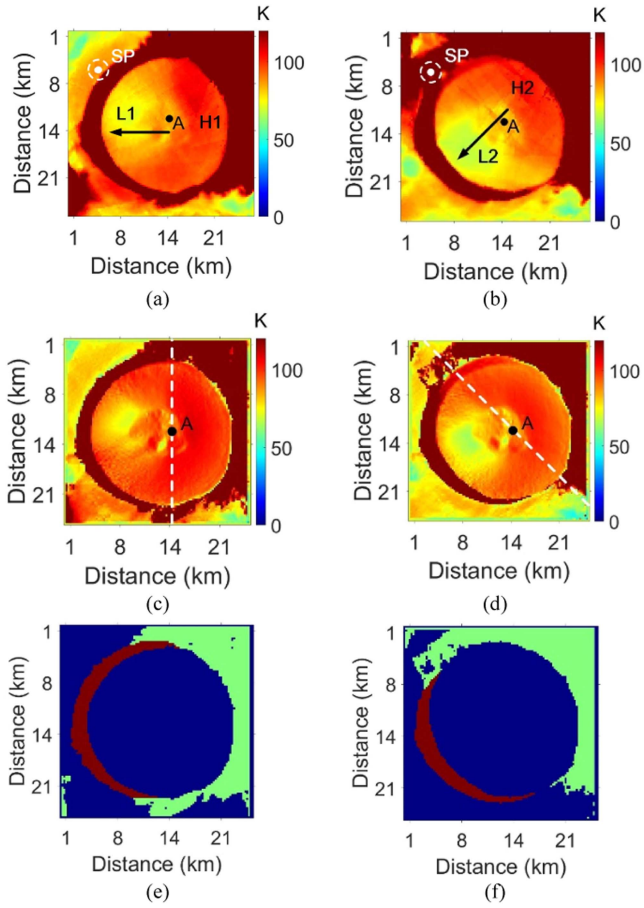
Fig. 4. Surface temperatures and sunlit regions of crater Shackleton at different local times in summer. (a) Diviner data at 14:30 obtained by averaging data of Diviner data with subsolar longitude of 82.5°, 86.25°, 90°, 93.75° and 97.5°. (b) Diviner data at 17:30 obtained by averaging data of Diviner data with subsolar longitude of 37.5°, 41.25°, 45°, 48.75°, and 52.5°. (c) Simulated surface temperature at 14:30 (UTC November 23th, 2028). (d) Simulated surface temperature at 17:30 (UTC April 16th, 2028). (e) Sunlit regions at 14:30. (f) Sunlit regions at 17:30. Blue represents regions in shadow, red represents the sunlit crater wall, and green represents other sunlit regions.

As shown in Fig. 1, the compiled Diviner data of [2] for a single subsolar point may not fully cover Shackleton [2]. The compiled Diviner data have a subsolar longitude interval of 3.75°. Fig. 4(a) and (b) are obtained by averaging the data of the adjacent subsolar longitudes of the central local time. The subsolar latitude of the simulated temperature at 14:30 is 1.50°S, and the subsolar latitude of the simulated temperature at 17:30 is 1.53°S. The black arrows in Fig. 4(a) and (b) indicate the directions of the direct sunlight. Comparing Fig. 4(a), (c) and (e) with Fig. 4(b), (d), and (f), it can be seen that the positions of sunlit crater walls influence the spatial temperature distribution within PSRs. High-temperature regions (H1, H2) in PSR are located on the crater walls facing the sunlit area in Fig. 4. Although the distances from the sunlit region to H1 and H2 are larger than low-temperature regions (L1, L2), the incident angles and emission angles of scattered and radiative heat fluxes from sunlit regions to H1 and H2 in Fig. 4 are smaller. So, the scattered and radiative heat fluxes are stronger, resulting in higher temperatures.

Point A has a temperature of 95.1 K at 14:30 in summer, which is higher than the temperature at 17:30 (89.0K). At 14:30, point A is located about 4.2 km from the center of the sunlit area, while the distance at 17:30 is about 3.8km. In both Fig. 4(c) and (d), the range of emission angles of thermal radiations from the sunlit region to point A is approximately between 75° to 90°, and the incident angle ranges from about 65° to 70°. The factors mentioned above have similar contributions to the temperature at point A.

As the lunar south pole is located in the upper-left area of crater Shackleton, when the sunlit region is closer to the south pole, the area and the temperature of the sunlit region reaches the maximum. As the sunlit region moves away from the south pole, the area of the sunlit region gradually decreases and the temperature drops as well. The sunlit crater wall is marked in red in Fig. 4(e) and (f), and other sunlit regions are marked in green. It can be seen that the area of sunlit crater wall at 14:30 [861 pixels in Fig. 4(e)] is larger than that at 17:30 [635 pixels in Fig. 4(f)].

The temperature of sunlit crater wall can reach 330 K at 14:30, while the maximum temperature at 17:30 is about 310 K. The larger areas of sunlit crater wall with higher temperatures are important reasons that result in higher heat fluxes received by point A. The scattered sunlight I_{SA} received by the lunar surface at point A at 14:30 is 2.0 W/m² and the thermal radiation I_{RA} is 2.8 W/m². At 17:30, the lunar surface at point A receives scattered sunlight I_{SA} of 1.5 W/m² and thermal radiation I_{RA} of 2.0 W/m². The varying areas and temperatures of the sunlit region at different local times during the daytime in summer are the important reasons for the diurnal temperature changes at point A.

The incident angles of heat fluxes and the lengths of the mechanical legs may affect the surrounding thermal environment. Since the solar incident angle θ_i of the sunlit crater wall ranges from 65° to 70°, if the height H_0 of the miniflyer in Fig. 3 is small, $\arctan(L_0/H_0)$ may exceed than θ_i, and the miniflyer may obstruct heat fluxes to the lunar regolith below, resulting in lower regolith temperatures beneath.

For point A located in the flat crater floor, the scattered and radiated heat fluxes from different directions that could be received by the miniflyer are further calculated. At 14:30, the region on the left part of the white dashed line in the crater in Fig. 4(c) contributes all the scattered sunlight I_{SA}^0. Thermal radiation I_{RA}^0 from the left part of the white dashed line in the crater is 6.4W/m², which is about 74% of the total thermal radiation. As a result, the heat fluxes received by the left surface of the miniflyer is much larger than that received by the right side. At 17:30, the thermal radiation I_{RA}^0 from the lower left part of the white dashed line in the crater to point A in Fig. 4(d) is about 4.7W/m², which is about 73% of the total thermal radiation. The huge differences of the heat fluxes from different directions will lead to an uneven temperature distribution on the surface of the miniflyer, which need to be considered in the design of the heating system of the miniflyer.

The miniflyer needs to land in a flat area within the PSR. Based on the slope map of Shackleton (see Fig. 2), four points (A–D) were selected for analysis. The simulations indicate that the
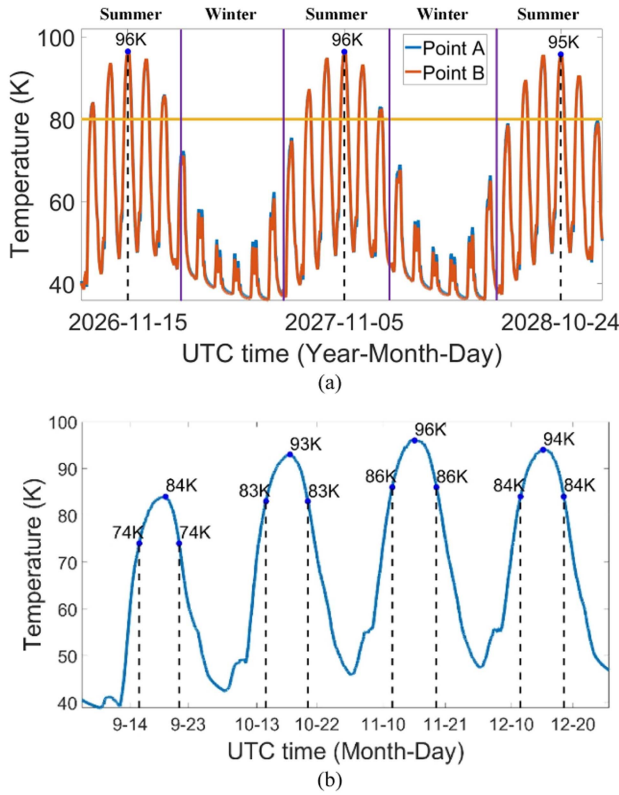
Fig. 5. Variations in the temperature of the flat crater floor of Shackleton during Chang'e 7 mission. (a) Variations in surface temperature at points A and B from September 2026 to December 2028. (b) Variations in surface temperature at point A from September to December 2026.

TABLE I
UTC TIMES WHEN TEMPERATURES ABOVE 80K AT POINT A FROM SEPTEMBER 2026 TO DECEMBER 2028

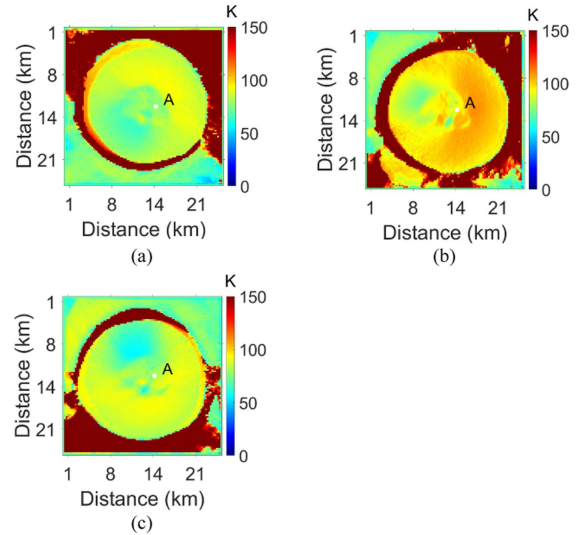| Year	2026	2027	2028
Month-Day	09-15 to 09-21	01-10 to 01-17	01-01 to 01-07
	10-12 to 10-23	09-04 to 09-12	08-23 to 08-31
	11-09 to 11-22	10-01 to 10-13	09-19 to 09-30
	12-09 to 12-21	10-30 to 11-12	10-19 to 10-31
		11-29 to 12-10	11-18 to 11-28

Fig. 6. Simulated surface temperatures of crater Shackleton in the duration of temperatures above 80K according to Table I. (a) UTC November 10th, 2026. (b) UTC November 15th, 2026. (c) UTC November 21th, 2026.

temperature variations at points A–D from September 2026 to December 2028 are similar. The temperature difference between points A and C is less than 2.9K, and the difference between points B and D is less than 3.9K. Among the four points, the maximum temperature difference is between points A and B, which is less than 4.3K. Therefore, Fig. 5(a) shows the change in surface temperature at points A and B from September 2026 to December 2028, with a time resolution of one earth hour. The seasons are defined based on the subsolar latitude. When the subsolar point is in the southern hemisphere, it is summer in the southern hemisphere; otherwise, it is winter.

Fig. 5(a) shows that the flat areas at points A and B experience diurnal and seasonal variations. The subsolar latitude varies periodically within the range of ±1.54° over a year. When the subsolar point is closer to the south pole, the solar incident angle in south pole region is smaller. The temperature of the direct sunlit crater wall is higher and the area of the sunlit region is larger. Therefore, the PSRs receive more scattered sunlight and thermal radiation, resulting in higher temperatures in PSR.

During the lunar summer in 2026, point A reaches maximum temperatures of 93 K in October and 94 K in December. On November 15, 2026, when the subsolar point is located at (1.54°S, 100.2°E), point A reaches its highest temperature of 96 K. During nights in summer, the sunlit area on the crater wall decreases, and the scattered sunlight and thermal radiation received by the PSRs diminish, reducing the temperature at

point A. The minimum nighttime temperature in the summer of 2026 ranges from 39 to 48 K. During the lunar winter in 2027, as the subsolar point moves toward the north pole, the area of the sunlit area on crater wall gradually decreases and the incidence angle of solar illumination increases, reducing the scattered and radiative heat flux received by the PSRs. Point A experiences lower temperatures during winter. Maximum temperatures of point A in winter are 47 K in May 2027 and 50 K in April and June 2027. The minimum nighttime temperatures are below 40 K. The cold temperatures within the PSRs result in thermal fatigue and require more energy for the temperature control of the miniflyer. Conducting missions during times with relatively warm temperatures reduce the rate of energy loss for the miniflyer.

Fig. 5(b) shows the temperature variations at point A from September to December 2026. The UTC time when the temperatures are within 10K from the peak temperature are marked in Fig. 5(b), lasting for about 9 to 11 days. Table I gives the UTC time when the surface temperatures are above 80K at point A from September 2026 to December 2028, which are suitable for conducting in-situ exploration missions in the PSRs. The duration of temperatures above 80K ranges from approximately 6 to 13 days. The surface temperatures of crater Shackleton in 2026 at UTC November 10th, November 15th, and November 21th are shown in Fig. 6, which is in the time window in Table I.
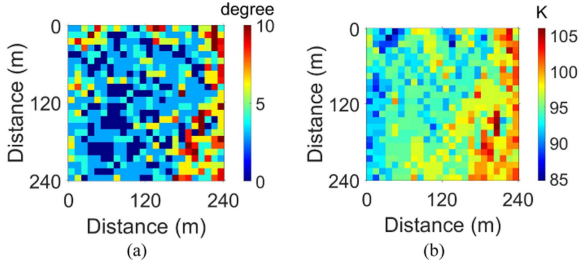
Fig. 7. Slope map and simulated temperature of the region around point A from DEM data of 10m/pixel. (a) Slope map of the region around point A with resolution of 10m/pixel. (b) Simulated surface temperature of the region around point A with resolution of 10m/pixel.

The spatial temperature in PSR varies during the time window in Table I because the direction of solar illumination changes.

The lunar surface temperature will be influenced by the shadow of the Earth, which is not included in the simulation. The duration of the Earth's occultation of the Moon (lunar eclipse), which occurs few times a year, is very short, usually lasting for several earth hours [24]. In addition, the lunar surface temperature can return to its pre-occultation level immediately after the end of the eclipse [24]. Therefore, the impact of the lunar eclipse is ignorable here.

The resolution of the DEM data will also have an impact on the simulation results. Flat regions with small slopes in the low-resolution DEM may contain complex topography in the high-resolution DEM. For example, the slope angle of point A in Fig. 2 is less than 5°. As shown in Fig. 7(a), the slope angles calculated from DEM data with resolution of 10m/pixel around point A range from 0° to about 10°.

To investigate the impact of DEM resolution on temperature simulation, DEM data around point A are replaced with high-resolution data for temperature simulation. According to the new result of ray tracing based on the high-resolution DEM, the scattered sunlight and thermal radiation received by regions around point A are calculated with the simulated temperature of crater Shackleton shown in Fig. 4(c). As the influence of subsurface conduction heat flux on temperature is much smaller than the received heat flow during daytime, the instantaneous temperatures around point A are simulated based on the received sunlight and thermal radiation [19], [25]

$$T = \left(\frac{I_R + I_S}{\overline{e} \cdot \sigma} \right)^{1/4} \quad (18)$$

where T is the surface temperature, I_R is the received thermal radiation, I_S is the received scattered sunlight, $\overline{e}$ is the hemispheric average emissivity and σ is the Stefan-Boltzmann constant.

The high-resolution temperatures around point A are shown in Fig. 7(b). In the low-resolution simulation, the temperature at point A is 95.1K, while the high-resolution data exhibits variations of ±10K in surface temperature due to changes in slope. However, for regions that remain flat in high resolution DEM, the simulated temperature is consistent with the low-resolution results.

IV. CONCLUSION

China's Chang'e 7 mission will conduct in-situ exploration within the PSRs. The thermal environment in PSR is one of the most important issues for the design of the miniflyer's internal heating system, the energy capacity, and mission time. Executing the mission during relatively warm temperature time can conserve energy and mitigate the adverse effects of cold-temperature environments. Therefore, predicting PSR temperatures is essential for estimating the energy required to maintain the temperature of the payloads. Variations in heat fluxes from different directions within the PSRs result in different heat flux intensities on surfaces of the miniflyer, thus influencing the design of thermal control system.

This article simulates the temperatures with high temporal resolution in the PSR of the crater Shackleton, which is the preferred landing site of Chang'e 7 mission. Diurnal temperature variations within the Shackleton crater are analyzed. The spatial temperature variations within Shackleton crater are studied as well. The heat fluxes from various directions to the miniflyer within the PSRs are different. Surfaces of miniflyer facing the directly sunlit region can receive more than 70% of the total heat flux. Surfaces with more heat flux reception require less power to maintain the temperature, which may influence the design of thermal control system.

Furthermore, this article presents the diurnal and seasonal temperature variations of flat crater floor in Shackleton's PSR between September 2026 and December 2028. Times when the temperatures are high in PSR during the summer on the Moon are provided. The time windows with relatively warm temperatures suitable for in-situ detection mission, such as the week after the midmonth in September and October in 2026, are recommended to reduce cold-related damage and conserver energy. This model can be applied to simulating the diurnal and seasonal temperatures on preferred landing sites in other PSRs as well.

REFERENCES

[1] D. A. Paige et al., "Diviner lunar radiometer observations of cold traps in the Moon's south polar region," *Science*, vol. 330, no. 6003, pp. 479–482, 2010.
[2] J. P. Williams et al., "Seasonal polar temperatures on the Moon," *J. Geophys. Res.. Planets*, vol. 124, no. 10, pp. 2505–2521, 2019.
[3] P. Gläser, A. Sanin, J. P. Williams, I. Mitrofanov, and J. Oberst, "Temperatures near the lunar poles and their correlation with hydrogen predicted by LEND," *J. Geophys. Res., Planets*, vol. 126, no. 9, 2020. [Online]. Available: https://doi.org/10.1029/2020JE006598
[4] N. Schorghofer and O. Aharonson, "The Lunar Thermal ice pump," *Astrophys. J.*, vol. 788, no. 2, 2014.
[5] W. Fa and Y. Cai, "Circular polarization ratio characteristics of impact craters from Mini-RF observations and implications for ice detection at the polar regions of the Moon," *J. Geophys. Res., Planets*, vol. 118, pp. 1582–1608, 2013.

[6] Y. Wang et al., "Lunar microwave imaging radar (LMIR)," in *Proc. 14th Eur. Conf. Synthetic Aperture Radar*, 2022, pp. 1–3.

[7] Y. Zou, Y. Liu, and Y. Jia, "Overview of China's upcoming Chang'E series and the scientific objectives and payloads for Chang'E 7 mission," in *Proc. 51st Annu. Lunar Planet. Sci. Conf.*, 2020, pp. 1755.

[8] N. Liu and Y.-Q. Jin, "Average infrared brightness temperature of lunar rough surface in field of view of high-resolution infrared radiation sounder and application to calibration," *IEEE Trans. Geosci. Remote Sens.*, vol. 60, 2022, Art. no. 4600312, doi: 10.1109/TGRS.2021.3094106.

[9] G. Wei et al., "Illumination conditions near the Moon's south pole: Implication for a concept design of China's Chang'E−7 lunar polar exploration," *Acta Astronautica*, vol. 208, pp. 74–81, 2023.

[10] Z. Yin, N. Liu, and Y.-Q. Jin, "Simulation of the temperatures in the permanently shadowed region of the Moon's south pole and data validation," *Icarus*, vol. 411, 2024, Art. no. 115917.

[11] P. R. M. Fisch and W. Whittaker, "Thermal management considerations for lunar polar micro-rovers," in *Proc. IEEE Aerosp. Conf.*, 2023, pp. 1–16.

[12] W. Chi et al., "Scientific objectives and payload configuration of the Chang'E-7 mission," *Nat. Sci. Rev.*, 2023, Art. no. nwad329.

[13] D. E. Smith et al., "The lunar orbiter laser altimeter investigation on the lunar reconnaissance orbiter mission," *Space Sci. Rev.*, vol. 150, pp. 209–241, 2010.

[14] J.-P. Williams, D. Paige, B. Greenhagen, and E. Sefton-Nash, "The global surface temperatures of the moon as measured by the diviner lunar radiometer experiment," *Icarus*, vol. 283, pp. 300–325, 2017.

[15] D. Paige et al., "The lunar reconnaissance orbiter diviner lunar radiometer experiment," *Space Sci. Rev.*, vol. 150, no. 1, pp. 125–160, 2010.

[16] P. O. Hayne et al., "Global regolith thermophysical properties of the moon from the diviner lunar radiometer experiment," *J. Geophys. Res., Planets*, vol. 122, no. 12, pp. 2371–2400, 2017.

[17] N. Liu and Y.-Q. Jin, "Simulation and data analysis of the temperature distribution and variation in the permanent shaded region of the Moon," *IEEE Trans. Geosci. Remote Sens.*, vol. 59, no. 4, pp. 2962–2972, 2020.

[18] A. R. Vasavada et al., "Lunar equatorial surface temperatures and regolith properties from the diviner lunar radiometer experiment," *J. Geophys. Res.*, vol. 117, 2012.

[19] G. D. Racca, "Moon surface thermal characteristics for moon orbiting spacecraft thermal analysis," *Planet. Space Sci.*, vol. 43, no. 6, pp. 835–842, 1995.

[20] N. Liu and Y.-Q. Jin, "A real-time model of the seasonal temperature of lunar polar region and data validation," *IEEE Trans. Geosci. Remote Sens.*, vol. 58, no. 3, pp. 1892–1903, Mar. 2020.

[21] V. Lohse, C. Heipke, and R. L. Kirk, "Derivation of planetary topography using multi-image shape-from-shading," *Planet. Space Sci.*, vol. 54, no. 7, pp. 661–674, 2006.

[22] R. Woods-Robinson, M. A. Siegler, and D. A. Paige, "A model for the thermophysical properties of lunar regolith at low temperatures," *J. Geophys. Res., Planets*, vol. 124, no. 7, pp. 1989–2011, 2019.

[23] A. Martinez and M. Siegler, "A global thermal conductivity model for lunar regolith at low temperatures," *J. Geophys. Res., Planets*, vol. 126, no. 10, 2021, Art. no. e2021JE006829.

[24] M. J. Burgdorf, N. Liu, S. A. Buehler, and Y.-Q. Jin, "Observation of a lunar eclipse at 89, 150, and 183 GHz," *Planet. Sci. J.*, vol. 4, no. 112, 2023, doi: 10.3847/PSJ/acd76e.

[25] T. Fang and W. Fa, "High frequency thermal emission from the lunar surface and near surface temperature of the Moon from Chang'E-2 microwave radiometer," *Icarus*, vol. 232, pp. 34–53, 2014.

Niutao Liu (Member, IEEE) was born in Jiangsu, China, in 1994. He received the B.S. degree in telecommunication engineering from Nangjing University of Posts and Telecommunications, Nanjing, China, in 2016, and the Ph.D. degree in electromagnetic field and microwave technology from Fudan University, Shanghai, China, in 2021.
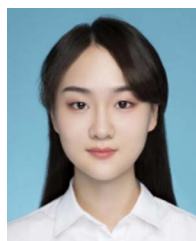
He is currently an Assistant Professor with the Key Laboratory for Information Science of Electromagnetic Waves (MoE), Fudan University. His research interests include microwave planetary remote sensing, infrared remote sensing, computational electromagnetics, and synthetic aperture radar data analysis.

Ya-Qiu Jin (Life Fellow, IEEE) received the Graduated degree in atmospheric physics from Peking University, Beijing, China, in 1970, and the M.S., E.E., and Ph.D. degrees from the Massachusetts Institute of Technology, Cambridge, MA USA in 1982, 1983 and 1985, respectively, all in electrical engineering and computer science.

He was the Research Scientist of Atmospheric Environmental Research, Inc., Cambridge, U.K., in 1985, a Research Associate Fellow of City University of New York, New York, U.K., in 1986–1987, and a Visiting Professor with University of York, York, U.K. in 1993 sponsored by the U.K. Royal Society. He has authored or coauthored more than 830 papers in refereed journals and conference proceedings and 17 books, including *Polarimetric Scattering and SAR Information Retrieval* (Wiley and IEEE, 2013), *Theory and Approach of Information Retrievals from Electromagnetic Scattering and Remote Sensing* (Springer, 2005), *Electromagnetic Scattering Modelling for Quantitative Remote Sensing* (World Scientific, 1994). His main research interests include electromagnetic scattering and radiative transfer in complex natural media, microwave satellite-borne remote sensing, as well as theoretical modeling, information retrieval and applications in earth terrain and planetary surfaces, and computational electromagnetics.

Dr. Jin was the recipient of the Senior Research Associateship in NOAA/NESDIS by USA National Research Council, 1996. He is currently the Te-Pin Professor and the Director of Key Laboratory for Information Science of Electromagnetic Waves (MoE), and Institute of EM Big data and Intelligence Remote Sensing, Fudan University, Shanghai, China. He is the Academician of Chinese Academy of Sciences, and a Fellow of TWAS (the World Academy of Sciences for Advances of Developing World), and International Academy of Astronautics. He was one of the first group of the IEEE GRSS Distinguished Speakers. He was co-Chair of TPC for IGARSS2011 in Vancouver Canada, and Co-General Chair for IGARSS2016 in Beijing, China. He was an Associate Editor for IEEE TRANSACTIONS ON GEOSCIENCE AND REMOTE SENSING (2005–2012), and IEEE ACCESS (2016–2018), the member of IEEE GRSS AdCom and the Chair for IEEE Fellow Evaluation of GRSS (2009-2011). He is currently the Member of IEEE GRSS Major Awards Committee. He was also the recipient of IEEE GRSS Distinguished Achievement Award (2015), IEEE GRSS Education Award (2010), the China National Science Prize (2011, 1993), the Shanghai Sci/Tech Gong-Cheng Award (2015), and the first-grade MoE Science Prizes (1992, 1996, and 2009) among many other prizes.

Zhengling Yin was born in Jiangsu, China, in 2000. She received the B.E. degree in artificial intelligence from Nangjing Agricultural University, Nanjing, China in 2022. She is currently working toward the M.S. degree in telecommunication engineering with the Key Laboratory for Information Science of Electromagnetic Waves (MoE) for Advanced Study, School of Information Science and Technology, Fudan University, Shanghai, China.

Her research interests include microwave planetary remote sensing and infrared remote sensing.